Optimization and an insightful properties—Activity study of electrospun TiO$_2$/CuO composite nanofibers for efficient photocatalytic H$_2$ generation

Siew Siang Lee, Hongwei Bai, Zhaoyang Liu, Darren Delai Sun*

School of Civil & Environmental Engineering, Nanyang Technological University, Singapore 639798, Singapore

ARTICLE INFO

ABSTRACT

Optimization of electrospun TiO$_2$/CuO composite nanofibers shows that TiO$_2$/CuO composite nanofibers with 6 mol.% Cu, calcined at 450 °C for 45 min, exhibited the highest H$_2$ generation from 10% (v/v) methanol aqueous solution. The significance of balance and synergy among the essential physicochemical properties such as morphology, porosity, specific surface area, degree of crystallinity, crystal size, as well as elemental states on the photocatalytic H$_2$ generation of electrospun TiO$_2$/CuO composite nanofibers was further revealed by means of varying the synthesis calcinations temperatures. Calcinations at temperature above and below 450 °C showed negative effect on the H$_2$ generation. This was ascribed to the temperature effect on transformation of crystalline phase, crystal growth, mesoporosity formation, and Cu valence state which has thus adversely affected the synergy among the physicochemical properties governing the photocatalytic activity of TiO$_2$/CuO composite nanofibers. Good stability with negligible Cu leaching and reusability were also attained with the composite nanofibers. This study serves as a significant advancement platform to designing and fabricating high efficient and stable TiO$_2$/CuO composite nanofibers via facile electrospinning thus promoting its application potential as an economical photocatalyst for production of clean energy.

© 2013 Elsevier B.V. All rights reserved.

1. Introduction

In response to the pressing global warming issue from the combustion of fossil fuel, hydrogen (H$_2$) as an ideal clean energy source has attracted large attention by researchers [1]. H$_2$ is a very attractive fuel source due to its zero carbon emission, high conversion efficiencies, and it can be easily produced and stored on site. It offers immense potential as a clean and renewable energy source which may alleviates the overdependence on fossil fuels. Photocatalytic H$_2$ generation from water splitting is one of the promising long-term solutions to generate H$_2$ [2–4] due to a few attributes: (1) it exploits the renewable solar energy with no threats of resource exhaustion; (2) it is emission-free thus there is low pollution risk and zero greenhouse gas effect [2,3], and (3) its system entails a relatively simple reactor setup.

TiO$_2$-based semiconductor has been widely-studied for H$_2$ production since it was first reported by Fujishima and Honda in 1972 [5–7]. Furthermore, TiO$_2$ is relatively inexpensive, non-toxic, and exhibits high chemical and thermal stability. However, TiO$_2$ has a wide band gap of 3.2 eV (anatase) which makes it hard to

be excited and inherent rapid recombination of photo-generated electron–hole pairs [8]. These drawbacks result in low photocatalytic activity of TiO$_2$ which impedes its practical application. Thus, in the past decades, significant effort has been devoted to designing and synthesizing new TiO$_2$-based functional materials so as to overcome the limitations of TiO$_2$ for sustainable energy applications.

TiO$_2$/CuO nanoparticles have been reported to show enhanced H$_2$ generation efficiency owing to the modified optical property which has enabled photon absorption from a broader range of the solar irradiation [9,10]. However, more work is still needed to improve TiO$_2$/CuO composite photocatalyst because nanoparticles have limitation in particular high aggregation tendency which leads to reduction in specific surface area for reaction [11]. Furthermore, aggregates could act as recombination centers for photogenerated charges thus impeding photocatalytic H$_2$ generation [3,12].

One-dimensional (1D) nanofibers could be a better option because it has low aggregation tendency and possesses high porosity, large specific surface area, and high aspect ratio [12] thus promoting efficient charge and mass transfer for high photocatalytic activity. There are many routes through which nanofibers can be fabricated such as hydrothermal, sol–gel, and electrospinning [13–15]. The former two methods require large amount of corrosive chemicals, high temperature, and more complex

synthesis steps. On the contrary, electrospinning followed by calcinations at high temperature could be a good synthesis approach to simplify the fabrication of ceramic nanofibers as it is a simple and relatively low-cost method [16]. Electrospun bare TiO_2 nanofibers has been reported elsewhere to exhibit better photocatalytic H_2 generation activity than that prepared via hydrothermal method because of better crystallinity and enhanced specific surface area [17]. Meanwhile, electrospinning of each pristine TiO_2 and CuO nanofibers have been widely reported in the open literature for their improved photocatalytic oxidation of organic pollutant [18,19]. Despite that, very little is done and known for electrospun TiO_2/CuO composite nanofibers in particular for H_2 generation. Hence, our group has developed and reported the successful fabrication of novel-structured TiO_2/CuO composite nanofibers which showed promising aspects in terms of improved H_2 generation efficiency as well as ease of recovery and reusability compared to its nanoparticles counterpart [10,20]. The TiO_2/CuO composite nanofibers, endowed with innovative physicochemical properties such as long nanofibrous structure, good mesoporosity, high specific surface area, small crystal size, large UV–vis light absorbance capability, as well as well-dispersed and closely contacted TiO_2/CuO heterojunctions, exhibited lower recombination of the photogenerated charges and narrower band gap which are advantageous for efficient photocatalytic reaction [20].

Moving forward, by varying the Cu content, this study strove to optimize the physicochemical properties of the TiO_2/CuO composite nanofibers to obtain the most efficient H_2 generation. Subsequently, by employing different calcinations temperatures during the synthesis [21,22], a comparative and an insightful investigation was carried out to relate the essential physicochemical properties such as morphology, porosity, specific surface area, crystal transformation, crystal size, UV–vis light absorbance and elemental state; with the final photocatalytic efficiency of the TiO_2/CuO composite nanofibers. Besides refining the preparation method and materials required to fabricate the most efficient and stable TiO_2/CuO composite nanofibers via facile electrospinning for clean energy production, this properties—photocatalytic activity relationship study is of paramount fundamental importance to understand and uncover the intriguing significance and interdependencies of the affected physicochemical properties toward the overall synergy and photocatalytic H_2 generation efficiency of the TiO_2/CuO composite nanofibers.

2. Experimental

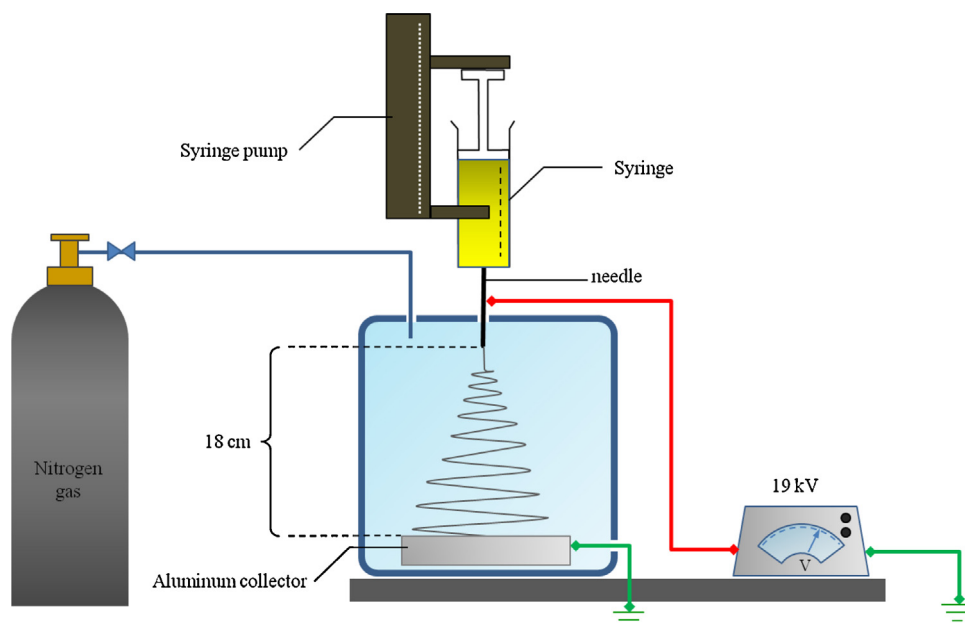### 2.1. Preparation of bare TiO_2 and TiO_2/CuO composite nanofibers

All chemicals were of analytical grades and used without further purifications. Both bare TiO_2 and TiO_2/CuO composite nanofibers were prepared according to the method as reported previously [20,23]. Briefly, 7 wt% of polyvinylpyrrolidone (PVP; M_w = 1 300 000) and 20 wt% of tetra n-butyl titanate ($Ti(oBu)_4$) were added into a solution comprising 4:1 ratio by volume of ethanol (CH_3CH_2OH) and acetic acid (CH_3COOH). The mixture was subsequently mixed for 6 h using magnetic stirrer to obtain a homogenous and clear precursor solution for bare TiO_2. Precursor solution for TiO_2/CuO composite was prepared by adding appropriate amount of copper 2-ethylethanoate ($Cu[CH_3(CH_2)_3CH(C_2H_5)CO_2]_2$) into the above mixture [20]. The composite containing 1 mol.% Cu, 3 mol.% Cu, 6 mol.% Cu, 9 mol.% Cu, and 12 mol.% Cu were labeled as TC-1, TC-3, TC-6, TC-9, and TC-12, respectively. Subsequently, the precursor solution was pumped at a rate of 0.3 mL/h through a hypodermic syringe with a 1.1 mm diameter stainless steel nozzle [18] which was subjected under a high electrical potential of 19 kV using a high voltage DC supply. The

distance between needle tip and aluminum foil collector was 18 cm. Scheme 1 illustrates the overall electrospinning setup. The enclosed electrospinning chamber was continuously purged with nitrogen (N_2) gas in order to prevent pre-mature hydrolysis of the precursor solution which can lead to formation of uneven nanofibers with beads [16,18]. The collected non-woven nanofibers webs were left in the air for 2 h for complete hydrolysis. Subsequently, the as-spun nanofibers were calcined in the air at 450 °C for 45 minutes in a furnace, at temperature rising rate of 0.5 °C/min to obtain TiO_2/CuO composite nanofibers and bare TiO_2 nanofibers. The propertiesactivity relationship study was undertaken using the TiO_2/CuO composite nanofibers with the Cu content which resulted in the most efficient photocatalytic H_2 generation. The as-spun TiO_2/CuO composite nanofibers were calcined in the air in a furnace at 350 °C, 450 °C, 550 °C, 650 °C and 750 °C for 45 min; and labeled as TC-350, TC-450, TC-550, TC-650 and TC-750, respectively.

TiO_2/CuO composite nanofibers were also fabricated via the conventional wet-impregnation (WI) method according to the procedure reported in our previous study [24] in order to compare with that synthesized via electrospinning method in terms of morphology, physical properties, optical properties, and photocatalytic H_2 generation efficiency. Copper (II) nitrate trihydrate ($Cu(NO_3)_2 \cdot 3H_2O$) was used as the precursor for Cu element. Deionized (DI) water was used to prepare the $Cu(NO_3)_2$ solution at the concentration appropriate to fabricate the composite photocatalyst with the most optimum Cu/Ti mol.% ratio. The electrospun bare TiO_2 nanofibers were added into the $Cu(NO_3)_2$ solution at a ratio of 0.2 g/10 ml. Subsequently, the mixture was subjected to ultrasonication for 2 h. The homogenous slurry was then dried in an oven at 103 °C overnight to remove the water and finally calcined at 450 °C for 4 h to obtain the final photocatalyst.

2.2. Characterization of bare TiO_2 and TiO_2/CuO composite nanofibers

The field-emission scanning electron microscopy (FESEM, JEOL JSM-7600F) coupled with high-end scanning transmission electron microscopy, STEM, was used to observe the morphology of the electrospun nanofibers. The accelerating voltage of the STEM was 30 kV. The microstructure of the nanofibers were further analyzed using the high resolution transmission electron microscopy (HRTEM, JEOL JEM-2010) working at an accelerated voltage of 200 kV. The Bruker D8 Advance X-ray diffractometer (XRD) with monochromated high-intensity Cu Kα radiation (λ = 1.5418 Å) was used to obtain the crystalline structure. The Scherrer Equation was used to estimate the crystal size according to the XRD pattern; whereby $L = K\lambda/\beta \cos\theta$ where L, K, $λ$, $β$, and $θ$ are size of particles in nm, a constant of 0.891, wavelength of X-ray, full width at half maximum (FWHM) of the XRD peak, and angle of diffraction, respectively [8,25]. The energy dispersive X-ray spectrometer (EDX) (Oxford Instrument, X-Max, 80 mm^2) attached to the FESEM (JEOL, JSM-7600F) was used to determine the elemental composition within the photocatalysts. The Thermo Scientific Evolution 300 UV–Vis spectrometer (Thermo Fisher Scientific, Massachusetts, USA) was used to record the absorption spectra of the photocatalysts. The Kubelka–Munk function was adopted to estimate new indirect bandgap of the photocatalysts [25,26]. It is the photon energy ($h\nu$) value when $[F(R_\infty)]^{0.5} = 0$, obtainable when the vertical segment of the plot of $[F(R_\infty)]^{0.5}$ against $h\nu$ is extended to intersect the x-axis ($h\nu$) [27]. The Fluorolog-3 spectrofluorometer (Horiba Scientific, New Jersey, USA) was used to carry out the PL analysis at an excitation wavelength of 300 nm [27]. The Micromeritics ASAP 2040 system was used to determine the Brunauer, Emmett, and Teller (BET) specific surface area at liquid nitrogen temperature (77 K). The sample was degassed at 200 °C for 3 hours prior to BET measurement. The pore size distribution was estimated by

Scheme 1. Schematic diagram of the electrospinning setup.

employing the Barret–Joyner–Halenda (BJH) method. The Kratos Axis Ultra Spectrometer with a monochromic Al Kα excitation source at 1486.7 eV, a voltage of 15 kV and an emission current of 10 mA, was used to determine the valence states of all elements via X-ray photoelectron spectroscopy (XPS). All binding energies were referenced to C 1s at 284.6 eV. Prior to calcinations, a Perkin Elmer thermogravimetric analyzer (TGA) model TGA7 was used to determine the thermal stability of the photocatalyst in the air across a range from 23 °C to 800 °C with a temperature increase rate of 5 °C/min.

2.3. Photocatalytic H_2 generation

The photocatalysts were suspended at a concentration of 0.5 g/L into 10% (v/v) methanol aqueous solution. Methanol aqueous solution was selected as it has been widely used and is one of the most efficient scavengers for photogenerated holes [2] thus enhancing charges separation and consequently the H_2 generation by photogenerated electrons. Photocatalytic H_2 generation test was carried out in an inner irradiation type Pyrex reactor with a 400 W high pressure Hg lamp (Riko, UVL-400HA) and 360 W high pressure Na lamp (Riko, HNL-360A) as the UV–vis light source [23] and visible light source, respectively. Dark adsorption–desorption equilibrium between the organic substrates and the photocatalysts was achieved after stirring for 30 min. A TCD-type gas chromatography (Agilent 7890A, HP-PLOT MoleSieve/5A) was used to measure the gas produced from the photocatalytic reaction [10,28]. This experiment was carried out in triplicate for each photocatalyst. The TiO$_2$/CuO composite nanofibers with an optimum Cu loading which gives the best H_2 generation was used in the subsequent study to investigate the properties-activity relationship under the effect of different calcinations temperatures. Similar characterizations and photocatalytic performance tests were employed for TiO$_2$/CuO composite nanofibers calcined at different temperatures. At the end of the 4-h reaction, an aliquot of 10 mL was sampled and filtered through a Millipore filter (0.45 μm). Subsequently, the filtered aliquot was measured for its total organic carbon (TOC) content. A Shimadzu TOC analyzer model TOC-V CSH was used to measure the TOC content of the sampled aliquot. The reacted photocatalysts were collected and dried overnight at 105 °C in an

oven. The regenerated composite nanofibers were re-used in the same reaction for 3 cycles to determine its stability and recyclability. The amount of Cu which was leached out after each reaction cycle was determined using an inductively coupled plasma optimal emission spectrometry (ICP OES) (Dionex ISC-1000) to further characterize the stability of the TiO$_2$/CuO composite nanofibers. pH value of the solution was measured by a Horiba F-53 pH meter. The effect of photocatalyst concentration on H_2 generation was also investigated to determine the optimum amount to be used. The as-prepared bare TiO$_2$ nanofibers and TiO$_2$/CuO composite nanofibers synthesized via WI method were also tested for H_2 generation for comparison.

3. Results and discussion

The results comprise primarily three parts: (1) preparation of the optimum TiO$_2$/CuO composite nanofibers, (2) the elucidation of physicochemical properties—H$_2$ generation activity relationship and (3) the stability and effect of photocatalyst concentration. Part 1 clarified the significant physicochemical properties influenced by the addition of different Cu content and determined the optimum Cu content within the TiO$_2$/CuO composite nanofibers for the most efficient H$_2$ generation from 10% (v/v) methanol aqueous solution, while Part 2 took on further to reveal the significance and interdependency of physicochemical properties in influencing the photocatalytic H$_2$ generation activity by employing different calcinations temperatures to prepare the optimum TiO$_2$/CuO composite nanofibers as determined in Part 1. The stability of the TiO$_2$/CuO composite nanofibers and the effect of photocatalyst concentration were covered in Part 3.

3.1. Preparation of the optimum TiO$_2$/CuO composite nanofibers

3.1.1. Characterization of TiO$_2$/CuO composite nanofibers

First of all, FESEM was employed to observe the morphology of the TiO$_2$/CuO composite nanofibers calcined at 450 °C for 45 min with different Cu contents. Observation by FESEM revealed that TC-1, TC-3, TC-6, TC-9 and TC-12 have similar surface morphologies. Fig. 1(a) and (b) shows representative morphology of the TiO$_2$/CuO composite nanofibers by TC-6. The diameter of the
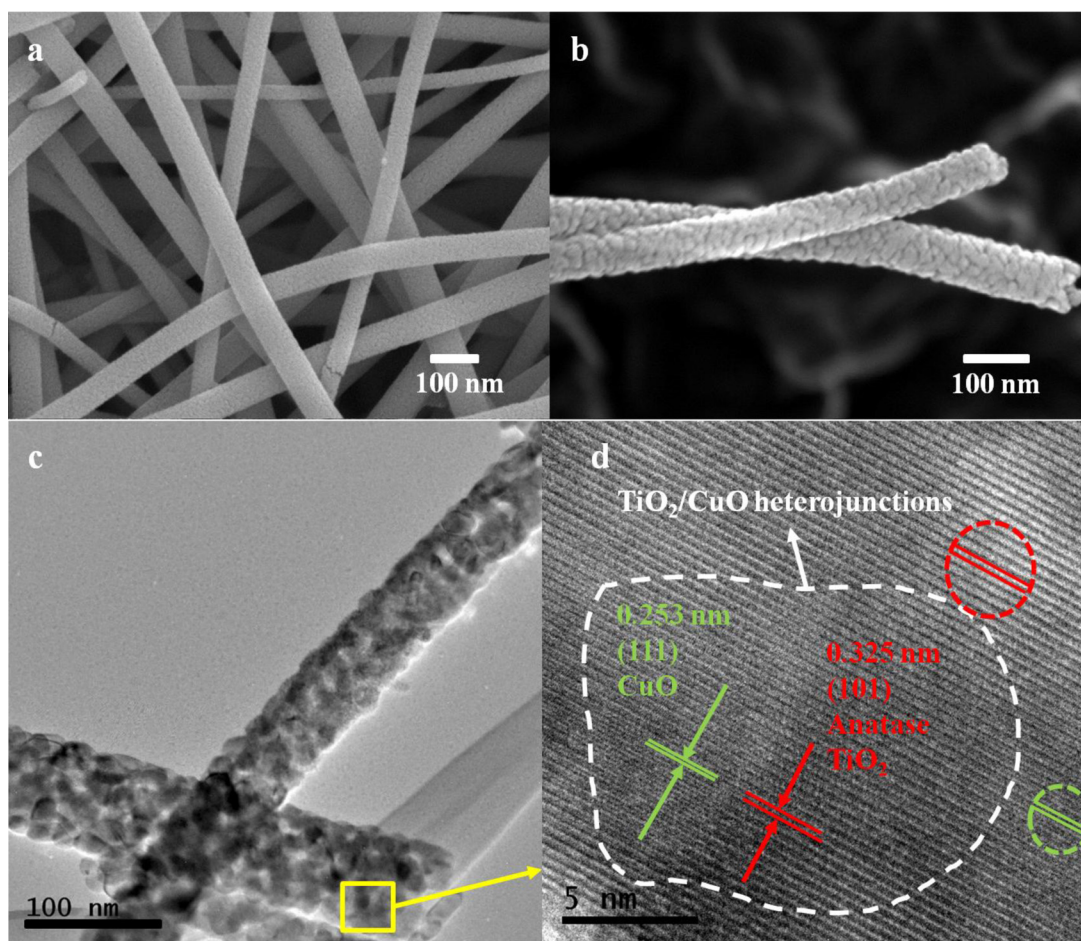
Fig. 1. (a) Low magnification FESEM images of TC-6 nanofibers, (b) high magnification FESEM image of TC-6 nanofibers showing detailed porous surface morphology, (c) bright field TEM image of TC-6 nanofibers, and (d) high magnification HRTEM image showing the corresponding crystal lattice of anatase TiO_2 and CuO from the delineated area in (c).

TiO_2/CuO composite nanofibers was consistently about 100 nm, with a length of more than 10 μm long and a typical aspect ratio of around 30–50. The humidity control using the N_2 gas has facilitated the elimination of beads as well as the formation of highly uniform structure because there was a sufficient control of precursor solution's surface tension which drives the formation of beads [29]. The surface of the TiO_2/CuO composite nanofibers appears to be very rough and porous in the high magnification FESEM image (Fig. 1(b)), thus indicating great potential for the improvement of the photocatalytic activity. Fig. 1(c) shows the microstructure of the electrospun TiO_2/CuO composite nanofibers observed by TEM. The HRTEM image as presented in Fig. 1(d) further elucidates that there were two distinctive lattice fringes of 0.325 nm and 0.253 nm which correspond well to the (101) plane of anatase TiO_2 [27] and the (1 1 1) plane of CuO, respectively [30,31].

The dark field FESEM-STEM image of TC-6 in Fig. 2(a) confirms that the TiO_2/CuO composite nanofibers were made up of granular nanocrystals. The brighter spots on the image could be attributed to the Cu element due to its heavier atomic weight compared to Ti [23]. The corresponding EDX spectrum in Fig. 2(b) shows that both Ti and Cu were present in the composite nanofibers. The mapping images as shown in Fig. 2(c)–(e) further support the co-existence of a well-dispersed Ti, Cu, and O elements. A good elemental dispersion would help optimize the elemental contact between the TiO_2 and CuO heterojunction, hence facilitating the migration of

electrons between conduction bands (CB) for more efficient photocatalytic reactions [32,33].

Fig. 3(a) illustrates the crystalline phase of the as-synthesized TiO_2/CuO composite nanofibers. CuO peak was not discernible at all in all of the composite nanofibers owing to relatively low Cu content, and the high dispersion of the Cu species within the photocatalysts as well-evidenced by the elemental mapping images in Fig. 3 [28,34]. High dispersion of Cu has resulted in low aggregation of Cu species thus yielding a dimension which was below the detection limit of XRD [35]. The composite nanofibers were all well-crystallized into anatase TiO_2 phase (JCPDS file No. 21-1272) [15]. The close-up XRD pattern in the region of $2\theta = 22$–$30°$ as shown in Fig. 3(b) clearly indicates the shift to a higher angle compared to that of the bare TiO_2 nanofibers. This observation was ascribed to the defect in the anatase TiO_2 crystal lattice due to the incorporation of Cu [36]. Approximation of the crystalline size using the Scherrer equation in Table 1 showed a reducing trend in the crystalline size of anatase TiO_2 from approximately 18 nm to 16 nm when Cu content increases, thus further corroborating that the addition of Cu has resulted in some degree of defects in the crystallization of the anatase TiO_2 [37]. Smaller crystal size is expected to benefit the photocatalytic reaction by increasing the availability of the photo-generated electrons and holes at the surface reaction sites due to a shorter migration distance [3].

A surface analysis using the N_2 adsorption–desorption isotherm technique demonstrated that TC-1, TC-3, TC-6, TC-9, and TC-12
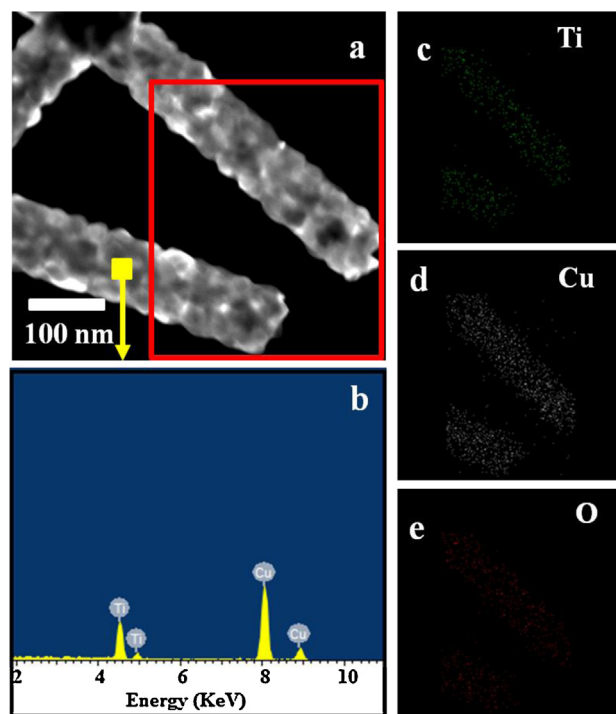
Fig. 2. (a) High magnification dark field FESEM-STEM image of two individual TC-6 nanofibers, (b) EDX spectrum of TC-6 nanofibers for the indicated point on TC-6 nanofibers in (a), elemental mapping images for the selected area in (a) for (c) Ti element, (d) Cu element, and (e) O element.

have similar curves. Fig. 4(a) shows a representative curve by TC-6 and bare TiO_2, which were type IV isotherm curve with obvious H3-type hysteresis [38]. Thus, the as-synthesized photocatalysts were all mesoporous [38], coupled with enhanced pore volume compared to that of bare TiO_2 nanofibers. The BJH analysis further affirmed the mesoporous nature of the TiO_2/CuO composite nanofibers since it showed a narrow pore size distribution of between 2 and 20 nm (Fig. 4(b)) [38]. As depicted in Table 2, the BET specific surface area of the composite nanofibers was significantly enhanced with increase in Cu content. This was consistent with the formation of smaller anatase TiO_2 crystals hence a higher specific surface area, due to the addition of Cu element. Consequently, an enhanced photocatalytic reaction could be expected since higher specific surface area would promote adsorption and mass transfer.

Fig. 5(a) illustrates the absorbance spectra of the TiO_2/CuO composite nanofibers in the UV–vis light region of between 350 and 800 nm. In general, increasing the Cu content has resulted in the increase of the absorption intensity in the UV and visible light
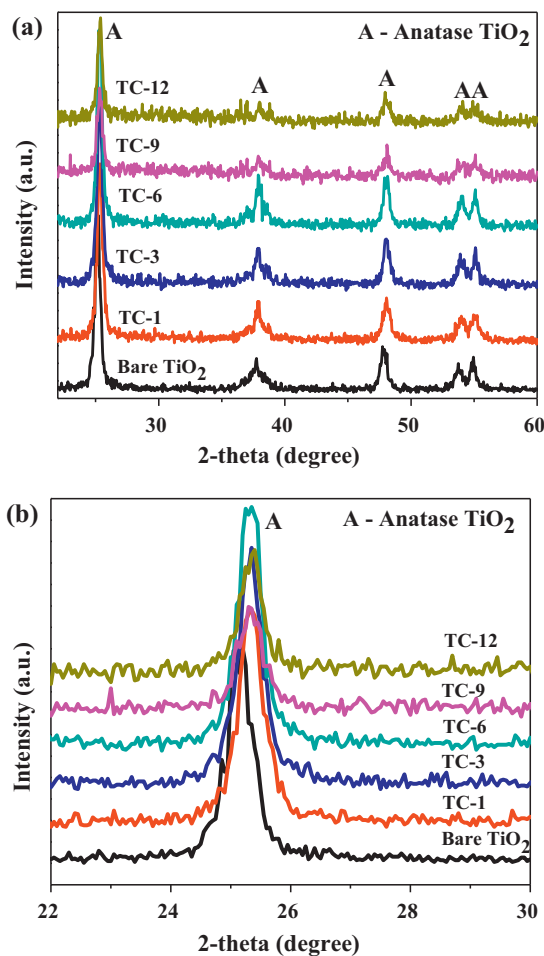

Fig. 3. (a) XRD patterns of TC-1, TC-3, TC-6, TC-9, and TC-12 nanofibers calcined at 450 °C for 45 min and (b) close-up XRD patterns for bare TiO_2 nanofibers, TC-1, TC-3, TC-6, TC-9, and TC-12 nanofibers calcined at 450 °C for 45 min ($2\theta = 22$–$30°$).

regions. In consistent with the XRD patterns (Fig. 3) and HRTEM image (Fig. 1(d)), the extension of the absorbance edge toward the visible light region by the TiO_2/CuO composite nanofibers suggested the successful incorporation of Cu element into the crystal lattice of anatase TiO_2 [39]. The red-shifting was attributed by the additional energy levels created by the Cu ions in the band gap of TiO_2 [39,40]. Consequently, there exists a transition from the valence band (VB) of the CuO to the conduction band (CB) of TiO_2 thus resulting in the significant narrowing of the TiO_2 bandgap energy as evidenced in the Kubelka–Munk analysis in

Table 1
Summary of physical properties of calcined bare TiO_2 nanofibers and TiO_2/CuO composite nanofiber.

Materials	FHWM (°)	Size of anatase crystal[a] (nm)
Bare TiO_2 nanofibers	0.443	18.2
TC-1	0.429	18.8
TC-3	0.463	17.4
TC-6	0.493	16.4
TC-9	0.497	16.2
TC-12	0.489	16.5
TC-350	0.450	17.0
TC-450	0.493	16.4
TC-550	0.319	25.3
TC-650	0.249	32.4
TC-750	0.176	45.8

[a] Calculated by the Scherrer equation [8,25].

Table 2
Summary of BET specific surface area for bare TiO_2 nanofibers and TiO_2/CuO composite nanofibers.

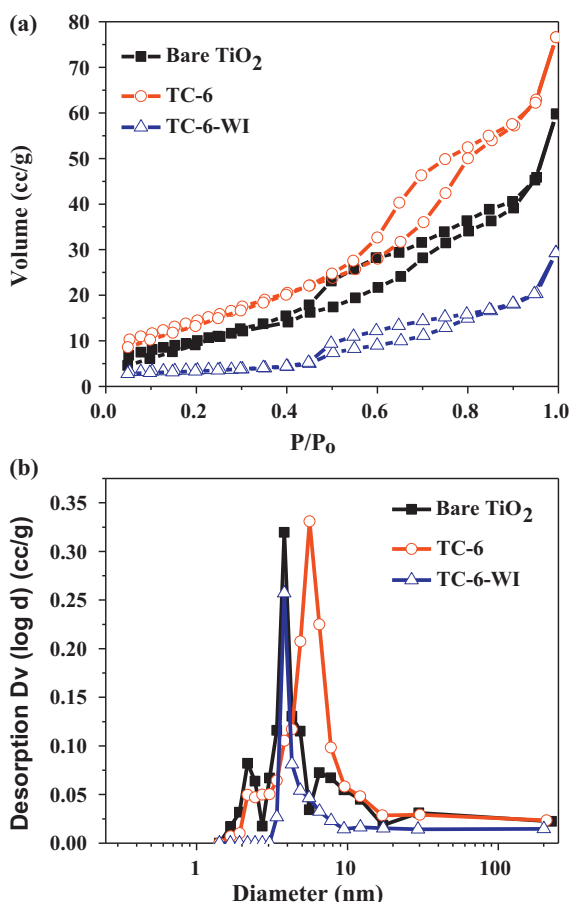| Materials	BET specific surface area (m²/g)
Bare TiO_2 nanofibers	34.30
TC-1	54.96
TC-3	56.38
TC-6	156.22
TC-9	108.14
TC-12	115.46
TC-6-WI	11.41
TC-350	73.78
TC-450	156.22
TC-550	120.40
TC-650	43.42
TC-750	17.85

Fig. 4. (a) N_2 adsorption/desorption isotherm curves of bare TiO_2 (red) nanofibers, TC-6 (black) nanofibers, and TC-6-WI (blue) nanofibers, and (b) BJH pore size distributions of bare TiO_2 (red), TC-6 (black) nanofibers, and TC-6-WI (blue) nanofibers. (For interpretation of the references to color in this figure legend, the reader is referred to the web version of the article.)

Fig. 5(b) [33]. The approximated indirect bandgaps for all of the as-synthesized TiO_2/CuO composite nanofibers were below 3.00 eV, with the narrowest being that of the TC-12 (Fig. 5(b)). This implies that the electronic structures of the pristine TiO_2 has been modified via the formation of the TiO_2/CuO heterojunctions [27] as well-witnessed by the HRTEM images in Fig. 1(d). Hence, coupled with the enhanced mesoporosity (Fig. 4) and specific surface area (Table 2) which promotes light absorption and reflection within the photocatalyst [41], the overall solar light absorption and utilization capability of the TiO_2/CuO composite nanofibers could be enhanced for a more efficient photocatalytic activity. This phenomenon could be further promoted by the good contact between TiO_2 and CuO heterojunction as witnessed by the high dispersion of Ti and Cu elements in Fig. 2(c)–(e). The enhanced light absorption capability will be advantageous for photocatalytic performance of the TiO_2/CuO composite nanofibers as the photogeneration of electrons–holes pairs will be greatly enhanced.

All TiO_2/CuO composite nanofibers showed distinctive PL signals following excitation at 300 nm. As shown in Fig. 6, there are three main emission peaks at approximately 400 nm, 435 nm, and 465 nm which corresponded to the band gap energy of 3.10 eV, 2.92 eV, and 2.67 eV, respectively. Thus, the dominant peak at 400 nm could be ascribed to the inter-bands PL phenomenon triggered by the light with energy equals to the band gap energy of anatase TiO_2 while the peaks at 435 nm and 465 nm could be attributed to band edge free excitons [36]. The surface oxygen vacancies and defects of the electrospun TiO_2/CuO
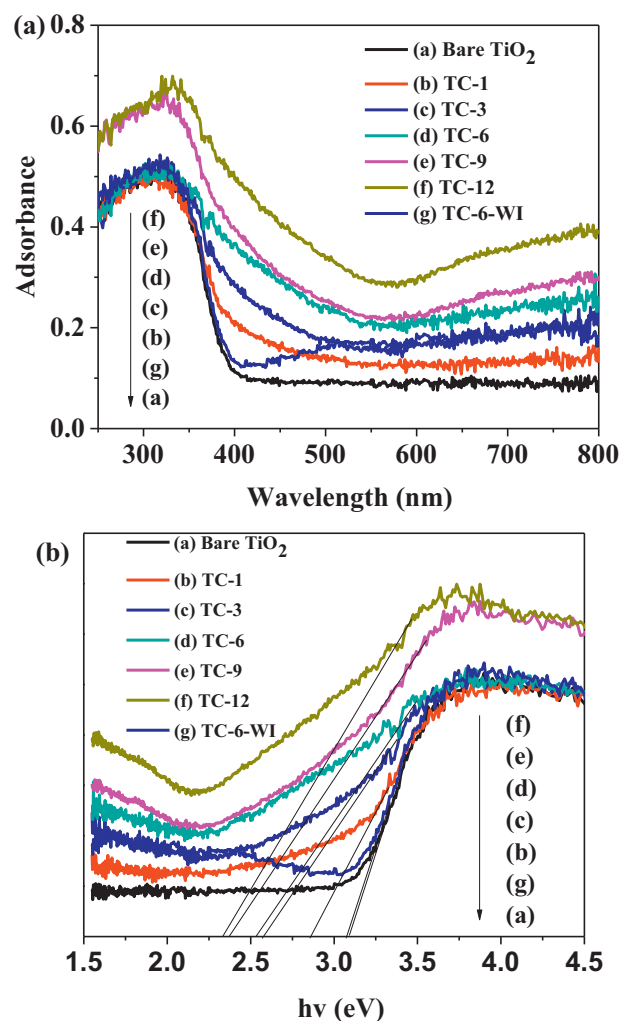

Fig. 5. (a) The UV–vis spectra of TC-1, TC-3, TC-6, TC-9, TC-12, and TC-6-WI nanofibers, and (b) the corresponding Kubelka–Munk transformed reflectance spectra to determine indirect new bandgap values for the as-synthesized TiO_2/CuO nanofibers.

composite nanofibers could result in the excitonic PL as witnessed from weaker peaks between 470 nm and 500 nm [36]. The effect of Cu addition was clearly demonstrated by the significantly lower PL spectra than that of the bare TiO_2 nanofibers. TiO_2/CuO
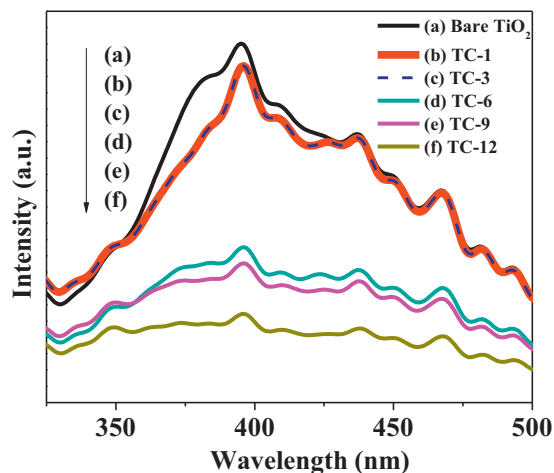

Fig. 6. Photoluminense spectra of TC-1, TC-3, TC-6, TC-9, TC-12 and bare TiO_2 nanofibers.
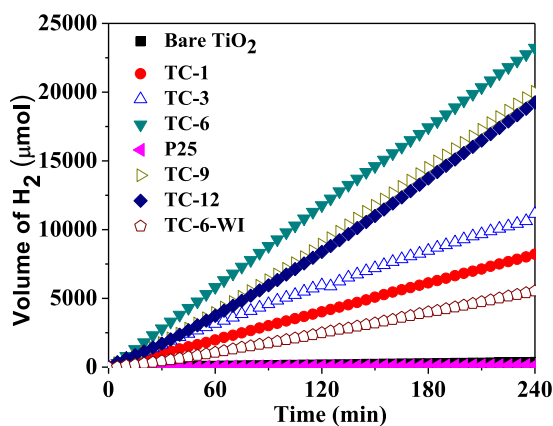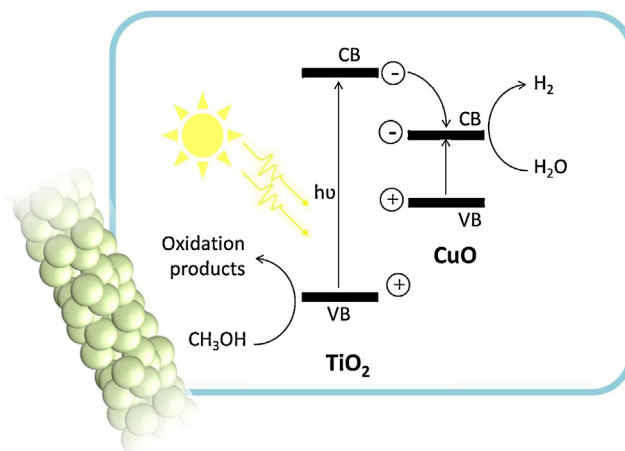
Fig. 7. Accumulation of photocatalytic H_2 evolution over the irradiation time of 4 hours over all as-synthesized TiO_2/CuO composite nanofibers.

Scheme 2. Schematic diagram of the photocatalytic H_2 generation over the TiO_2/CuO heterojunctions.

composite nanofibers are therefore expected to exhibit fast separation between photogenerated electrons and holes since lower PL spectra intensity indicates lower recombination tendency of the photogenerated charges [27]. In the TiO_2/CuO heterojunctions, a different energy potential existed between the CB of TiO_2 and that of the CuO, thus promoting the migration of the photogenerated electrons from CB of TiO_2 to that of CuO and hence minimizing the recombination possibility of the photogenerated electrons and holes. Among all the TiO_2/CuO composite nanofibers, both TC-1 and TC-3 have the highest PL spectra, indicating their highest recombination tendency. This could be addressed by the relatively low Cu content in TC-1 and TC-3 which resulted in a weak effect of TiO_2/CuO heterojunctions in facilitating photogenerated charges separation. On the other hand, TC-6, TC-9, and TC-12 possessed higher Cu content for the formation of TiO_2/CuO heterojunctions which promote transfer of the photogenerated charges.

3.1.2. Photocatalytic H_2 production

Photocatalytic H_2 generation of the as-prepared TiO_2/CuO composite nanofibers with bare TiO_2 nanofibers used as control was evaluated in a 10:1 (v/v) water–methanol mixture. The solution pH values before and after the 4-h reaction were measured to be 6 and 5, respectively. As illustrated in Fig. 7, an immense enhancement of H_2 production over the composite nanofibers in comparison to bare TiO_2 nanofibers was demonstrated. The amount of evolved H_2 increased with increasing Cu content up to 6 mol.%. The highest evolution of H_2 occurred with TC-6, approximated to be 23,000 μmol, which was 15 times higher than that of the bare TiO_2 nanofibers. Compared to the bare TiO_2 nanofibers, the enhanced pore volume and larger specific surface area of the TiO_2/CuO composite nanofibers as witnessed from the BJH and BET analysis in Fig. 4 and Table 2 respectively have increased the reaction sites availability thus facilitating reactants adsorption and interfacial charge transfer to the adsorbed substrates [8,12,17]. Furthermore, the smaller anatase TiO_2 crystal size following the incorporation of Cu (Table 1) offered a shorter migration distance for the photogenerated charges thereby promoting faster accessibility to the reaction sites and enhancing the initiation of the photocatalytic reaction [3]. The extended light sensitivity into the visible light region (Fig. 5) have also contributed to the improved photocatalytic capability of TiO_2/CuO composite nanofibers. Besides the improved physicochemical and optical properties of the TiO_2 photocatalyst, the photocatalytic H_2 production over the electrospun TiO_2/CuO composite nanofibers was enhanced also due to the TiO_2/CuO heterojunctions (Fig. 1(d)). The heterojunctions (1) promote charge

separation and extend their lifespan for photocatalytic activity by facilitating migration of photogenerated electrons from CB of TiO_2 to CB of CuO as evidenced in Fig. 6 and (2) contain CuO which serves as the co-catalyst by rendering the reduction sites for H_2 production [36,42,43]. Due to the lower H_2O reduction potential than that of the CB of CuO, the electrons migrated from CB of TiO_2 will be quickly lost for H_2 production. The good distribution of CuO on the surface as well as the bulk of the host semiconductor (TiO_2) (Fig. 2) coupled with the enhanced mesoporosity (Fig. 4(a)) have allowed greater accessibility of the reactants to the TiO_2/CuO heterojunctions for a more efficient photocatalytic reaction. Meanwhile, the reddish color appearance of the suspension at the end of the photocatalytic reaction suggested that there was reduction of surface CuO to Cu_2O or Cu^0 during the irradiation due to photoreduction [28,44] thus implying that there was competition for photogenerated electron with proton for its reduction into H_2 [28]. Nonetheless, it is postulated that the photoreduction of CuO into Cu_2O or Cu^0 which consumes electrons exhibited negligible impact on H_2 generation since Cu_2O and Cu0 are also co-catalysts for photocatalytic H_2 generation [10] and there was no significant reduction in H_2 evolution as seen in Fig. 7. Upon drying in the air and subsequently in the oven, the Cu_2O or Cu^0 were easily oxidized back into CuO as the photocatalysts powder turned into blackish color [10]. The highly dispersed and closely contacted Ti and Cu as depicted in Figs. 2(c)–(e) further promoted the rapid migration of photogenerated electrons such that the CB of CuO served only as an interim location for the photogenerated electrons from TiO_2 hence retarding the photoreduction and dissolution of CuO, which enhance the photocatalysts' stability for reuse [45]. Hence, considering the experimental observation and electrons transfer mechanism which occurred in the TiO_2/CuO composite nanofibers system, even though CuO could be possibly photoreduced, this reaction was not detrimental to the overall H_2 generation efficiency because: (1) CuO, Cu_2O and Cu^0 are all capable to co-catalyze photocatalytic H_2 production and (2) TiO_2/CuO heterojunctions were highly stable given the high dispersion and heterojunctions proximity which could also accelerate the transfer of photogenerated charges such that CuO photoreduction which leads to dissolution or leaching could be minimized. Scheme 2 illustrates the basic mechanism of photocatalytic H_2 generation which takes place over the TiO_2/CuO composite nanofibers.

On the contrary, despite the enhanced BET specific surface area, mesoporosity, visible light absorption capability and photogenerated charges separation, the rate of H_2 generation removal showed a decreasing trend in TC-9 and TC-12 possibly due to

the coverage of the host TiO_2 semiconductor by CuO which could limit the light accessibility thus limiting the initiation of photo-catalytic reaction [46]. In addition, the relatively higher crystalline defects of the anatase TiO_2 due to the higher Cu inclusion could contribute to the overall decrease in the photocatalytic H_2 generation by TC-9 and TC-12 because crystal defects are potentially charges recombination centers thus could retard the charges separation and subsequently weaken the photocatalytic performance [47].

It is worthy to note that the H_2 evolution of TC-6 was observed to be 2 times higher than that of the TiO_2/CuO nanoparticles which were synthesized by our group via the WI method [10]. In order to make a more relative comparison to elucidate the advantage of the facile electrospinning method, the conventionally used WI method was employed to synthesize TiO_2/CuO composite nanofibers where electrospun bare TiO_2 nanofibers were impregnated with 6 mol.% Cu (hereinafter referred to as TC-6-WI). The FESEM, EDX spectrum and elemental mapping images of TC-6-WI (Fig. S1 and Fig. S2) as attached in the Supplementary Information (SI) evidenced the successful addition of CuO onto TiO_2 nanofibers through WI method. As shown in Fig. 7, TC-6 exhibited H_2 evolution which was 4 times higher than that of TC-6-WI. Even though the long nanofibrous structure was sustained with good surface dispersion of Cu, TC-6-WI was synthesized at the expense of porosity and pore volume as shown Fig. 4(a) and (b). This could be ascribed to the adsorption of Cu elements onto the TiO_2 nanofibers. Subsequently, the BET specific surface area of the TC-6-WI as shown in Table 2 was greatly reduced when compared to that of the electrospun bare TiO_2 nanofibers. While enhanced photoresponse into the visible region of the irradiation spectrum was observed, there was negligible shift of the absorbance edge by TC-6-WI as shown in Fig. 5(a), thus implying that CuO was only deposited on the surface and not incorporated into the lattice of anatase TiO_2 [36,48]. This observation coincides with that reported previously in other literature [24]. Therefore, the crystallization of anatase TiO_2 was not affected by Cu addition in TC-6-WI and this was further corroborated by the absence of specific surface area and mesoporosity enhancement as oppose to that seen in TC-6. Meanwhile, the TiO_2 bandgap energy was slightly lowered for TC-6-WI following the Kubelka–Munk analysis (Fig. 5(b)) likely due to the addition of CuO which absorbs both UV and visible lights [39]. Unlike the WI method which entails separate precursor solution preparation steps for the electrospinning of bare TiO_2 nanofibers and impregnation of Cu respectively, the innovative single-step precursor solution preparation prior to electrospinning has enabled a good elemental mixing at molecular scale between Ti and Cu thus enabling the doping of Cu into the TiO_2 crystal lattice [49] for enhancement of the physicochemical properties as well as facilitating the formation of highly dispersed and closely-contacted TiO_2/CuO heterojunctions at molecular scale on both the surface and bulk of the semiconductor structure. As such, the relatively lower photocatalytic H_2 generation efficiency of TC-6-WI compared to that of TC-6 could be attributed mainly to: (1) the loss of specific surface area thus reducing the reactants adsorption capability of TC-6-WI, (2) the reduced porosity thus posing difficulty in the diffusion of reacting molecules through the porous network [47], (3) the relatively lower light absorption and utilization capabilities because the optical property was not greatly enhanced in TC-6-WI and the reduced specific surface area and porous structure were less favorable for light reflection and absorption, and (4) lack of closely-contacted TiO_2/CuO heterojunctions to facilitate charge transfer. In general, in this study, electrospinning method was found to offer the advantage of heterojunctions proximity and distribution, as well as process simplicity and time over WI method since highly enhanced TiO_2/CuO composite nanofibers can be easily synthesized in just one-step facile electrospinning.
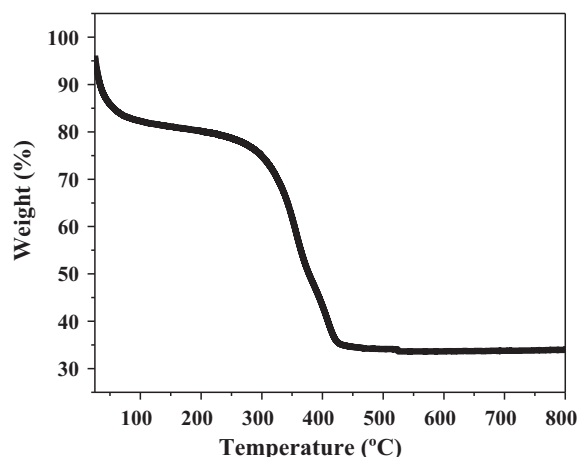

Fig. 8. TGA curve for uncalcined TC-6.

3.2. Elucidation of physicochemical properties – H_2 generation activity relationship

TiO_2/CuO composite nanofibers with 6 mol.% Cu (TC-6) which exhibited the highest H_2 generation as discussed in Section 3.1.2 was used to further investigate the influence and interdependency of physicochemical properties on the photocatalytic H_2 generation activity of the photocatalyst.

The thermogravimetric analysis (TGA) was first performed on the uncalcined as-spun PVP/Ti(oBu)$_4$/Cu[CH$_3$(CH$_2$)$_3$CH(C$_2$H$_5$)CO$_2$]$_2$ composite nanofibrous mat to determine the thermal stability of the photocatalyst prior to calcinations. Fig. 8 illustrated the TGA curve of TC-6 in the air across a range of 25–800 °C with temperature increase rate of 5 °C/min. Three distinctive phases of weight loss could be deduced: (1) between 25 and 100 °C – loss of moisture adsorbed by the as-spun nanofibrous web from the atmosphere [50], (2) between 100 and 300 °C – loss of water molecules originated from the chemicals used and throughout the synthesis process [50], and (3) between 300 and 450 °C – loss of polymer and organic [50]. No further weight loss was observed from 450 to 800 °C. The TGA curve was the basis from which the calcinations temperatures of investigation were determined.

3.2.1. Effect of calcinations temperatures on physicochemical properties

Prior to relating the physicochemical properties and the H_2 generation activity, the influence of calcinations temperature on physicochemical properties were first identified and clarified. Fig. 9(a)–(e) illustrated the STEM-FESEM images which clarified the microstructure of the photocatalysts. While no significant temperature effect on the surface morphology was observed in a report by Wu on pristine TiO_2 nanorods [50], in this study, the STEM-FESEM images vividly showed that as the calcinations temperature increases, the surface of the TiO_2/CuO composite nanofibers have evolved from a non-porous surface structure (Fig. 9(a)), into a very rough and porous surface (Fig. 9(b) and (c)), and finally into a smooth-surfaced structure with diminishing porosity (Fig. 9(d) and (e)). Higher temperature could promote fusion and growth of the granular nanocrystals into larger crystals [50] thus possibly resulting in a smoother surface structure. Nevertheless, the overall morphology remained long regardless of the calcinations temperature.

The increase of calcinations temperature has resulted in an enhanced degree of crystallization as evidenced by the growingly sharpening peaks of the XRD patterns as illustrated in Fig. 10
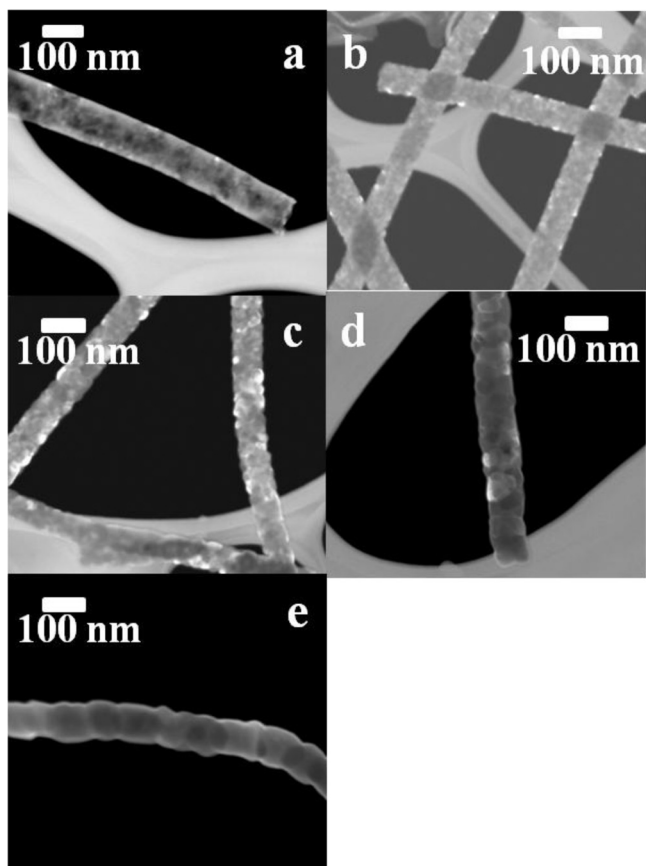
Fig. 9. High magnification STEM-FESEM images for (a) TC-350, (b) TC-450, (c) TC-550, (d) TC-650, and (e) TC-750.

[50], which was further affirmed by the narrowing of full width at half maximum (FHWM) with elevating temperature as shown in Table 1. Good crystallinity is essential to ensure minimum defects within the crystal structure thus ensuring fast separation of photogenerated charges [3]. In addition to anatase TiO_2 phase (JCPDS file No. 21-1272) [15], peaks corresponding to rutile TiO_2 and CuO started to appear at 450 °C and beyond. Additional Cu_2O phase on top of rutile TiO_2 and CuO was obvious in the XRD pattern of TC-750. The most intensified peaks for rutile TiO_2 (JCPDS file
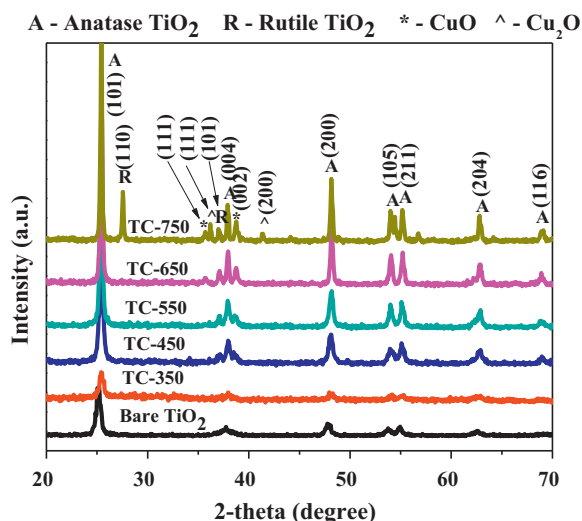

Fig. 10. XRD patterns of TC-350, TC-450, TC-550, TC-650, and TC-750 nanofibers.
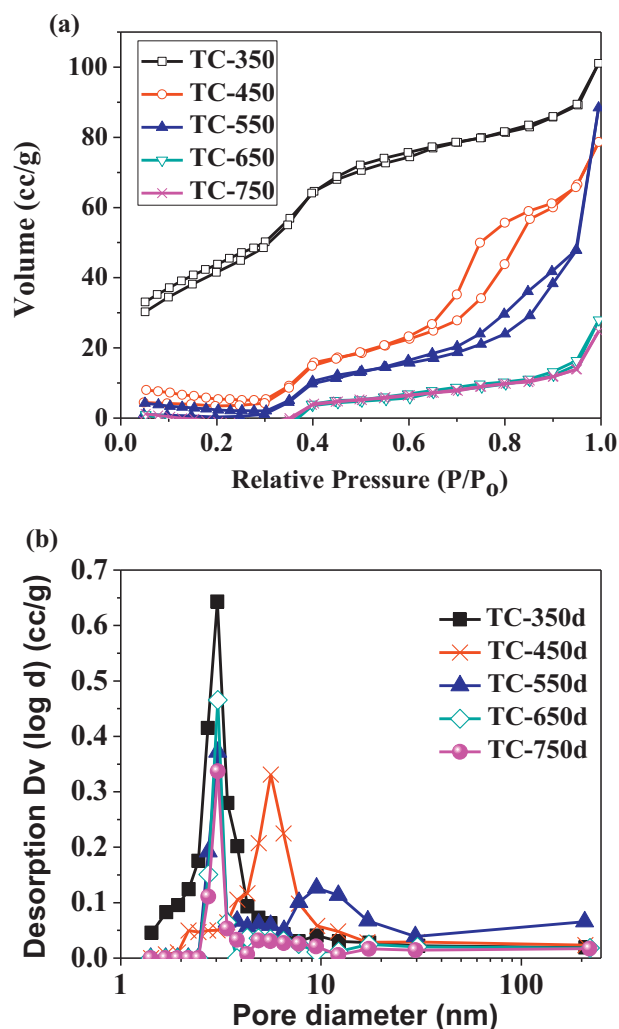

Fig. 11. (a) N_2 adsorption/desorption isotherm curve of TiO_2/CuO composite nanofibers calcined at different temperatures, and (b) BJH pore size distributions of TiO_2/CuO composite nanofibers calcined at different temperatures.

No. 21-1276) [15], CuO (JCPDS file No.48-1548) [51] and Cu_2O (JCPDS file No. 74-1230) [52] were located at $2\theta = 37°$ (1 0 1), 38.8° (0 0 2), and 36.5° (1 1 1), respectively. In addition to grayish and blackish shades, TC-550, TC-650, and TC-750 nanofibers exhibited increasing intensity of red shade as temperature increases suggested the existence of CuO and Cu_2O in the photocatalysts. Higher temperature could induce the phase transformation of CuO into Cu_2O as Cu^{2+} was reduced to Cu^+ [52]. Similar observation was also reported by Lalitha et al. where CuO and Cu_2O were formed at low and high calcinations temperature, respectively [39]. Nonetheless, Wu et al. demonstrated an opposite phenomenon whereby CuO was synthesized at 450 °C and beyond [53]. Different synthesis routes and chemicals employed could possibly address the discrepancies observed in the resulting photocatalysts. Meanwhile, based on the Scherrer equation, the crystal size was found to increase with the temperature (Table 1), with the highest being that of TC-750 which was approximated to be 45.8 nm. This estimated trend was consistent with the observed morphology using STEM-FESEM in Fig. 9(a)–(e) whereby the granular nanocrystals were enlarged thus resulting in a smoother surface at higher temperature.

A report by Bueno-Ferrer et al. (2010) demonstrated that larger crystals exhibit lower specific surface area [54]. Likewise in this study, TC-750 had the least specific surface area as well-corroborated by the measured BET specific surface area as depicted
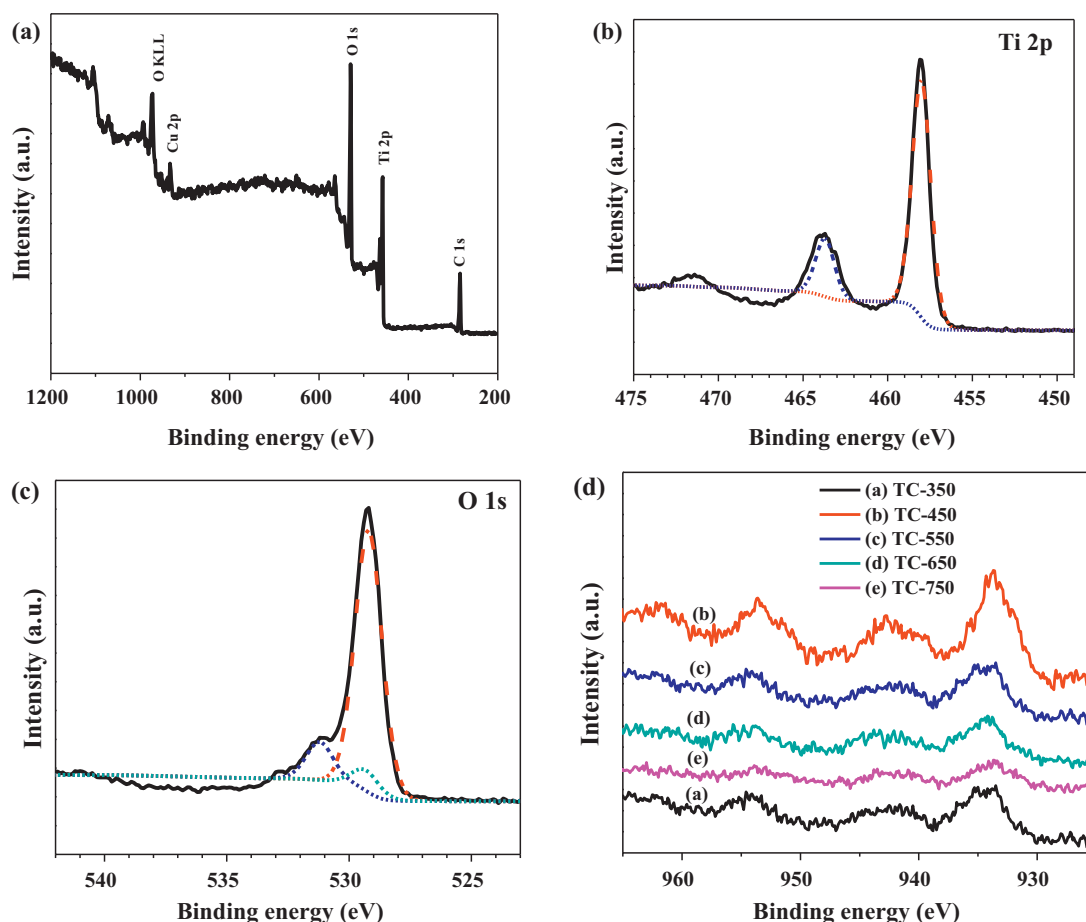
Fig. 12. (a) XPS survey spectrum for TC-450 nanofibers; high resolution XPS spectrum of TC-450 nanofibers for (b) Ti 2p, (c) O 1s, and (d) Cu 2p.

in Table 2. Both TC-450 and TC-550 have the highest specific surface area, implying enhanced adsorption capability for mass transfer. Meanwhile, the N_2 adsorption–desorption isotherm technique showed that TC-350 was not mesoporous (Fig. 11(a)), which was in good agreement with the rather smooth surface morphology as shown in Fig. 9(a). Since PVP removal under high temperature is one of the contributing factors for porosity formation [18], the presence of polymer at 350 °C as witnessed by the TGA curve in Fig. 8 could address the incomplete transformation of the nanofibers with porous structure hence yielding a smooth surface. Disappearance of mesoporosity was also observed in TC-650 and TC-750 due to the growth of crystals which has diminished the pores. This was clearly illustrated in Fig. 9(a)–(e) and thus also addressed the decreasing specific surface area from TC-350 to TC-750 (Table 2). Only both TC-450 and TC-550 were mesoporous. Hence, specific surface area of TC-350 could be endowed by its large aspect ratio, while the significantly high specific surface area of TC-450 and TC-550 were possibly given by the enhanced mesoporosity coupled with the large aspect ratio. Mesoporous structures also play an important role in facilitating fast diffusion of reactants to enhance the photocatalytic reaction [55]. Fig. 11(b) shows the pore size distributions of TC-6 calcined at different temperatures. Unlike TC-450 and TC-550 which possessed larger pore size of between 6 and 12 nm, TC-350, TC-650 and TC-750 exhibited smaller pore size peaking at 3 nm thus further corroborating the absence of mesoporosity (Fig. 11(a)) due to the incomplete formation of porous nanofibers in TC-350 as well as the enhanced crystal growth at higher calcinations temperature in TC-650 and TC-750 [50].

The XPS analysis was employed to determine the chemical states of all the elements in TC-6 calcined at different temperatures, in particular Ti and Cu. The binding energy for C1s peak at 284.6 eV was used as the reference for calibration. Fig. 12(a) is the typical survey spectrum by TC-450 and it confirms that Ti, Cu, and O were present in the composite nanofibers. The valence state for Ti remained +4 for all photocatalysts as evidenced by the peaks at the binding energy of 458.0 eV and 464.0 eV which were indicative of Ti $2p_{3/2}$ and Ti $2p_{1/2}$, respectively (Fig. 12(b)). Meanwhile, as shown in Fig. 12(c), the peaks at binding energy of 529.5 eV was the evidence of O 1s in TiO_2 and CuO or Cu_2O [28]. A high resolution spectrum for Cu 2p in Fig. 12(d) implies that the valence state of Cu could have been changed with temperature. TC-350, TC-450 and TC-550 exhibited peaks around the binding energy of 933.9 eV and 953.9 eV ascribing to the Cu $2p_{3/2}$ and Cu $2p_{1/2}$ of Cu^{2+} in CuO [49], respectively. The obvious characteristic shakeup satellite peaks around 942.0 eV and 962.0 eV further confirmed the existence of Cu^{2+} in TC-350, TC-450 and TC-550 [56]. On the other hand, in TC-650 and TC-750, despite the presence of peak at 933.9 eV and its shakeup peaks at 942.0 eV, the peak at 953.9 eV with its corresponding shakeup peaks at 962.0 eV have weakened. Based on the XRD pattern in Fig. 10 and the reddish shade of the photocatalysts, the co-presence of Cu^+ and Cu^{2+} might be the reasonable cause for the diminishing Cu^{2+} peaks at high temperature for TC-650 and TC-750 despite no obvious XPS peak was observed for Cu^+ possibly due to its low content [53,57]. The valence state of Cu element may result in a different photocatalytic performance of the TiO_2/CuO composite nanofibers [52].

3.2.2. Interplay between physicochemical properties on H_2 generation activity

Fig. 13(a) clearly illustrates the effect of calcinations temperature thus the influence of physicochemical properties on photocatalytic H_2 generation. TC-450 appeared to be the most efficient among others, with the highest H_2 generation rate of 5800 μmol/h. Incorporated with the high magnification FESEM images of TC-350, TC-450, TC-550, TC-650, and TC-750, an overview of how the physicochemical properties have changed with the calcinations temperature was given in Scheme 3 in order to vividly illustrate the interdependency between physicochemical properties for H_2 generation. TC-450 possesses beneficial integration of (1) mesoporosity with high specific surface area which enables high reactants accessibility, diffusion and adsorption, (2) good crystallinity thus minimum defects for efficient charge transfer, (3) enhanced light absorption capability thus facilitating photogeneration of charges, as well as (4) crystal size small enough to promote accessibility of the surface reaction sites by the photogenerated charges [47]. On the contrary, TC-550, regardless being comparable with TC-450 in terms of mesoporosity, specific surface area, and light absorption capability, exhibited better crystallinity thus resulting in a larger crystal size (Table 1). Even though good crystalline structure is favorable for charges transfer [47], the large crystal size may be detrimental to the overall photocatalytic performance due to the longer migration distance that needed to be overcome by the photogenerated charges in order to reach the surface reaction sites. Moreover, TC-550 has less mesopores volume (Fig. 11(a)) compared to TC-450 thus has less efficient mass transfer through the photocatalysts which could limit the photocatalytic reaction [55].

The importance of a good synergy between major physicochemical properties as exhibited in TC-450 become more significant when both TC-650 and TC-750 demonstrated remarkably lower H_2 generation efficiency than that of TC-450 and TC-550 due to the negative effects from the small specific surface area, large crystal size and absence of mesoporosity which has dominated the enhanced charge transfer efficiency effect from the higher degree of crystallinity. Likewise, TC-350 which was not mesoporous with low crystallinity, exhibited the least photocatalytic efficiency because lacked adsorption, diffusivity and charge transfer efficiency albeit possessing small crystal size. Meanwhile, the higher H_2 generation rate over TC-750 compared to TC-350 suggested that degree of crystallinity could a more dominant factor than specific surface area in driving the photocatalytic H_2 generation. However, since the synergy of more than one physicochemical properties determines the overall photocatalytic efficiency, there would be a limit where a much higher degree of crystallinity at the expense of excessive specific surface area could retard the final H_2 generation efficiency, such as that seen in TC-750 compared to TC-650. While Cu_2O has been reported to be the active site for photocatalytic H_2 generation [24,39,53], the presence of Cu_2O alone may not be sufficient in enhancing the overall photocatalytic performance as observed in TC-550, TC-650 and TC-750 owing to the absence of other positive factors in particular optimum specific surface area, mesoporosity, and appropriate crystal size. This study suggested that CuO is also an active reaction site and does not inhibit photocatalytic H_2 generation as that reported before [53] since CuO was solely observed in TC-450 (Figs. 10 and 12(b)) which exhibited the highest photocatalytic capability.

The photocatalytic H_2 generation efficiency over TC-6 under sole visible light was also investigated to bolster the value of TC-6 as prospective photocatalysts for renewable clean energy production. TC-450 and TC-750 were used for this study owing to the different dominance of CuO and Cu_2O which have different bandgap energies [9] and both photocatalysts possessed the extreme characteristics and properties of both ends (Scheme 3). Negligible H_2 generation

was observed when bare TiO_2 nanofibers were used under the visible light irradiation. As depicted in Fig. 13(b), both TC-450 and TC-750 exhibited encouraging H_2 evolution rate of approximately 720 μmol/h and 180 μmol/h, respectively, thus implying that with an appropriate calcinations temperature, TC-6 could be a potential photocatalysts for H_2 production under the renewable solar irradiation. The relatively much lower H_2 generation rate under the visible light activation compared to that under the UV–vis light could be attributed to the reduced irradiation spectrum thus lowering the degree of activation and probability for photogeneration of electrons and holes, especially when TiO_2/CuO composite nanofibers possessed an overall more intense absorbance in UV light region than that of visible light region as illustrated in Fig. 5. Similar H_2 generation trend under UV–vis light and visible light was also reported by Maeda et al. [43]. Besides showing that both CuO and Cu_2O could function efficiently in the TiO_2/CuO heterojunctions as the co-catalysts for H_2 generation under both UV–vis and visible lights irradiation, the importance of synergy of the physicochemical properties was again highlighted since TC-450 exhibited higher H_2 generation than TC-750 even under the activation of merely the visible light.

In addition to H_2 generation, concurrent TOC removal was observed to determine how the physicochemical properties influence the photocatalytic oxidation reaction which occurs in tandem with the photocatalytic H_2 generation. The overall TOC removal trend (Fig. 13(c)) shows that the best physicochemical properties synergy for H_2 generation was also true for the photocatalytic oxidation of the methanol. As shown in Fig. 13(c), the highest TOC removal at the end of the 4-h reaction was also observed over TC-450, approximated to be 12%. This non-detrimental effect is favorable as methanol degradation involves the consumption of photogenerated holes which helps prevent recombination of photogenerated electrons and holes thus increasing the availability of photogenerated electrons for H_2 generation. While adsorption thus specific surface area has been pointed out as the essential property in driving the photocatalytic oxidation of organic compound [3], the lower TOC removal over TC-550 compared to that over TC-450 despite both having relatively higher specific surface areas has further implied that the larger crystal size of TC-550 could exert some negative effect on the overall photocatalytic efficiency. TC-350 has obviously lost its photocatalytic oxidation efficiency to the absence of mesoporosity as well as the low degree of crystallinity. However, endowed with a higher specific surface area which facilitated adsorption and mass transfer, TC-350 exhibited a relatively similar TOC removal as TC-650. Even though the good crystallinity possessed by both TC-650 and TC-750 could enhance the separation of photogenerated electrons and holes, the relatively similar TOC removal between TC-350, TC-650 and TC-750 as shown in Fig. 13(c) has implied that the negative effects from the much reduced specific surface area and lost of mesoporosity were more dominant. In brief, the overall TOC removal observation has further reinforced the proposed significance of physicochemical properties synergy on the photocatalytic efficiency of the as-synthesized TiO_2/CuO composite nanofibers.

3.3. Stability and effect of photocatalyst concentration

TC-450 was easily recovered and re-used for photocatalytic H_2 production under the same condition. As shown in Fig. 14(a), no appreciable loss of photocatalytic performance was observed for TC-450 albeit being used for 3 cycles. The prospect of recovery and reusability of a photocatalyst is one of the crucial factors in determining the viability of using the photocatalyst for water treatment. Unrecoverable photocatalyst after a treatment process may result in a secondary pollution of the effluent water thus posing potential threat to human health and that of the ecosystem. What is more,
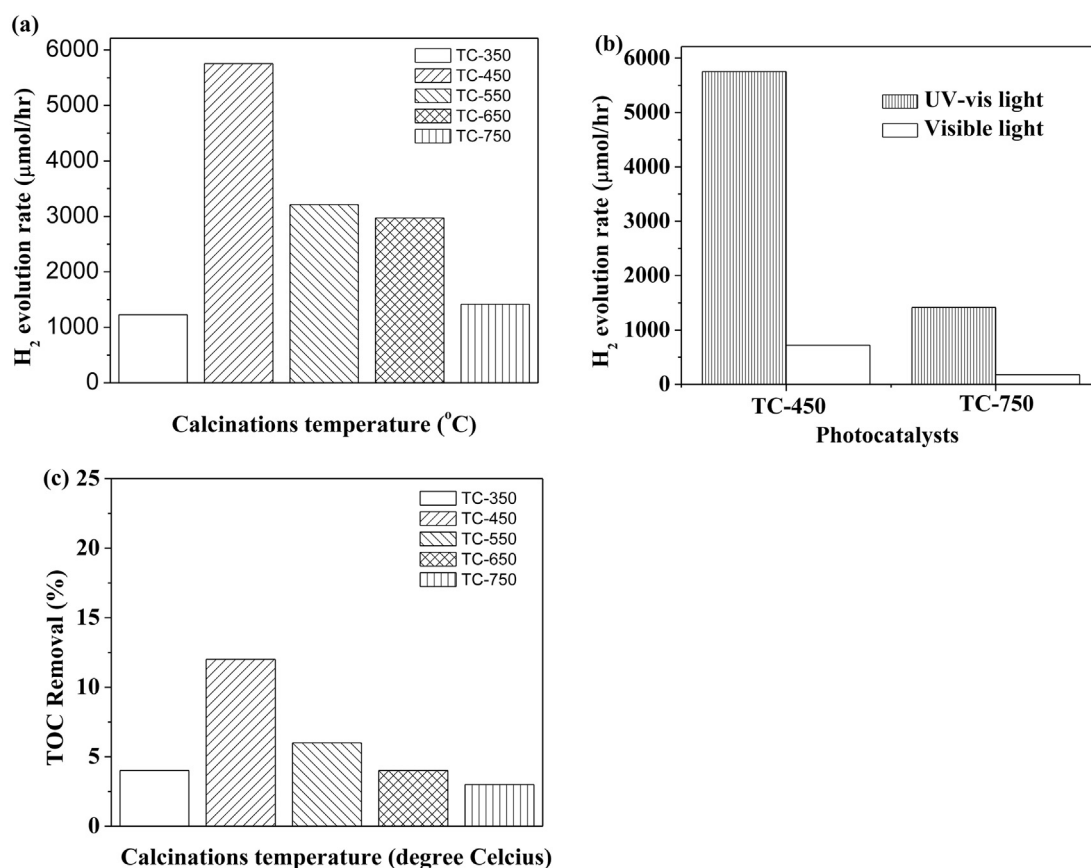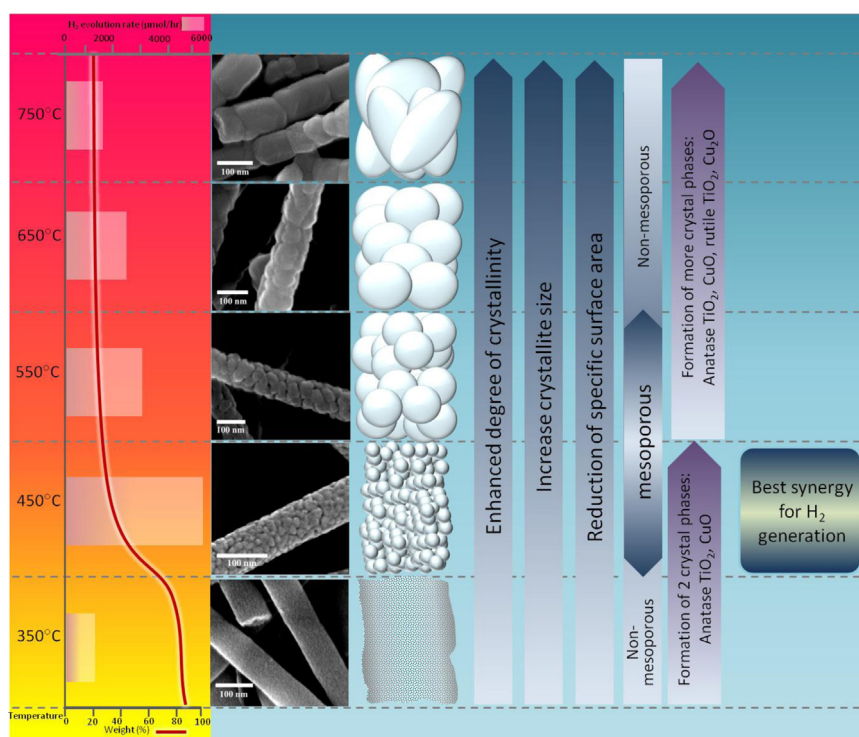
Fig. 13. (a) Dependence of H_2 evolution rate on the calcinations temperature in photocatalysts, (b) comparison of H_2 evolution rate between UV–vis light and visible light over TC-450 and TC-750 and (c) dependence of TOC removal (%) on the calcinations temperature in photocatalysts.

Scheme 3. Schematic of the effect of calcinations temperatures on the physicochemical properties.
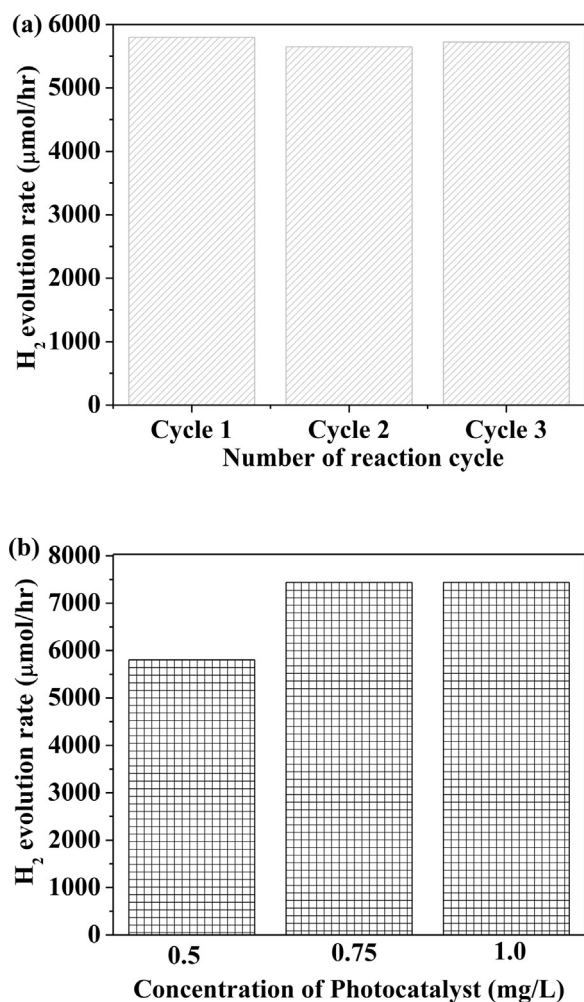
Fig. 14. (a) Reusability experiment for photocatalytic H_2 generation by TC-450 and (b) effect of TC-450 nanofibers concentration on the H_2 evolution rate.

Cu ion was not detectable in the reacting solution after every cycle thus implying another milestone of improvement as Cu leaching from a photocatalyst has been one important environmental concern impeding the use of this composite system for wastewater treatment. The as-synthesized TiO_2/CuO composite nanostructure and its fabrication method could have rendered the TiO_2/CuO composite system with a greater stability. In this study, the employed electrospinning method has enabled an optimized chemical usage where good elemental contact and high dispersion hence low agglomeration of Cu elements within the TiO_2/CuO composite nanofibers could be attained. Consequently, Cu leaching was minimized as it could be strongly held within the matrix of host TiO_2 photocatalyst instead of merely on its surface [24]. On the contrary, approximately 1.0 ppm of Cu was detected in the reacted solution following the 4-h photocatalysis reaction over TC-6-WI, further signifying the advantage of electrospinning method which produced inseparable TiO_2/CuO heterojunctions with high dispersion and close contact for an efficient charges transfer [45]. This marked a great improvement of the photocatalyst's stability compared to that from our previously developed CuO-incorporated TiO_2 nanoparticles and nanotubes which also lacked demonstration on their reusability [10,28]. Meanwhile, the photocatalyst concentration could influence the photocatalytic generation of H_2 generation. Fig. 14(b) illustrates that the optimum concentration was 0.75 g/L.

Higher concentration of the photocatalyst may inhibit the light accessibility and utilization due to increased reflection [53].

4. Conclusion

In summary, the optimum Cu content that facilitated the best photocatalytic H_2 generation over TiO_2/CuO composite nanofibers was determined to be 6 mol.%. By varying the calcinations temperatures, physicochemical properties such as the surface morphology, porosity, specific surface area, crystalline phase transformation, degree of crystallinity, crystal size and the elemental valence state, were observed to be interdependent and have jointly affected the photocatalytic H_2 generation efficiency of the as-synthesized photocatalysts. TiO_2/CuO composite nanofibers with 6 mol.% Cu and calcined at 450 °C for 45 min exhibited the highest photocatalytic H_2 generation without compromising the simultaneous TOC removal ascribing to the apt synergy of mesoporosity, specific surface area, well-dispersed and closely-contacted TiO_2/CuO heterojunctions for efficient charge separation, enhanced photoresponse into the visible light range, suitable crystallinity and crystal size. This synthesis route also implies energy saving since low calcinations temperature was found to be sufficient to yield efficient TiO_2/CuO composite nanofibers. The as-synthesized nanofibers photocatalysts can be easily recovered and re-used with sustained efficiency and negligible Cu leaching. This study has witnessed the vivid changes of physicochemical properties under the influence of different calcinations temperatures on top of their importance and synergy in governing the advantage of electrospun TiO_2/CuO composite nanofibers and has provided a good fundamental for research advancement using electrospun TiO_2/CuO composite nanofibers to generate clean energy.

References

[1] Z. Zou, J. Ye, K. Sayama, H. Arakawa, Nature 414 (2001) 625–627.
[2] X. Chen, S. Shen, L. Guo, S.S. Mao, Chemical Reviews 110 (2010) 6503–6570.
[3] A. Kudo, Y. Miseki, Chemical Society Reviews 38 (2009) 253–278.
[4] N. Getoff, International Journal of Hydrogen Energy 15 (1990) 407–417.
[5] A. Fujishima, K. Honda, Nature 238 (1972) 37–38.
[6] L. Kruczynski, H.D. Gesser, C.W. Turner, E.A. Speers, Nature 291 (1981) 399–401.
[7] A.A. Nada, M.H. Barakat, H.A. Hamed, N.R. Mohamed, T.N. Veziroglu, International Journal of Hydrogen Energy 30 (2005) 687–691.
[8] X. Chen, S.S. Mao, Chemical Reviews 107 (2007) 2891–2959.
[9] N. Helaïli, Y. Bessekhouad, A. Bouguelia, M. Trari, Journal of Hazardous Materials 168 (2009) 484–492.
[10] S. Xu, D.D. Sun, International Journal of Hydrogen Energy 34 (2009) 6096–6104.
[11] P. Le-Clech, E.K. Lee, V. Chen, Water Research 40 (2006) 323–330.
[12] S.K. Choi, S. Kim, S.K. Lim, H. Park, Journal of Physical Chemistry C 114 (2010) 16475–16480.
[13] T. Nonoyama, T. Kinoshita, M. Higuchi, K. Nagata, M. Tanaka, K. Sato, K. Kato, Journal of the American Chemical Society 134 (2012) 8841–8847.
[14] C. Bian, Y. Yu, G. Xue, Journal of Applied Polymer Science 104 (2007) 21–26.
[15] Z. Liu, D.D. Sun, P. Guo, J.O. Leckie, Nano Letters 7 (2007) 1081–1085.
[16] D. Li, J.T. McCann, Y. Xia, M. Marquez, Journal of the American Ceramic Society 89 (2006) 1861–1869.
[17] S. Chuangchote, J. Jitputti, T. Sagawa, S. Yoshikawa, ACS Applied Materials & Interfaces 1 (2009) 1140–1143.
[18] D. Li, Y. Xia, Nano Letters 3 (2003) 555–560.
[19] V. Gombac, L. Sordelli, T. Montini, J.J. Delgado, A. Adamski, G. Adami, M. Cargnello, S. Bernai, P. Fornasiero, Journal of Physical Chemistry A 114 (2010) 3916–3925.
[20] S.S. Lee, H. Bai, Z. Liu, D.D. Sun, Water Research, 2013, http://dx.doi.org/10.1016/j.watres.2012.12.044
[21] A. Kubacka, G. Colóon, M. Fernáández-Garcíía, Applied Catalysis B: Environmental 95 (2010) 238–244.

[22] Q. Zhang, L. Gao, J. Guo, Applied Catalysis B: Environmental 26 (2000) 207–215.

[23] S.S. Lee, H. Bai, Z. Liu, D.D. Sun, International Journal of Hydrogen Energy 37 (2012) 10575–10584.

[24] S. Xu, J. Ng, X. Zhang, H. Bai, D.D. Sun, International Journal of Hydrogen Energy 35 (2010) 5254–5261.

[25] B. Ohtani, Chemistry Letters 37 (2008) 217–229.

[26] Z. Liu, H. Bai, D. Sun, Applied Catalysis B: Environmental 104 (2011) 234–238.

[27] J. Ng, S. Xu, X. Zhang, H.Y. Yang, D.D. Sun, Advanced Functional Materials 20 (2010) 4287–4294.

[28] S. Xu, A.J. Du, J. Liu, J. Ng, D.D. Sun, International Journal of Hydrogen Energy 36 (2011) 6538–6545.

[29] D. Li, Y. Xia, Advanced Materials 16 (2004) 1151–1170.

[30] M. Cao, C. Hu, Y. Wang, Y. Guo, C. Guo, E. Wang, Chemical Communications 9 (2003) 1884–1885.

[31] P.I. Gouma, J. Lee, Journal of Nanomaterials 2011 (2011).

[32] L.S. Yoong, F.K. Chong, B.K. Dutta, Energy 34 (2009) 1652–1661.

[33] X. Bokhimi, A. Morales, O. Novaro, T. Lóópez, O. Chimal, M. Asomoza, R. Góómez, Chemistry of Materials 9 (1997) 2616–2620.

[34] H. Sayilkan, Applied Catalysis A: General 319 (2007) 230–236.

[35] S. Xu, J. Ng, A.J. Du, J. Liu, D.D. Sun, International Journal of Hydrogen Energy 36 (2011) 6538–6545.

[36] J. Yu, J. Ran, Energy and Environmental Science 4 (2011) 1364–1371.

[37] S. Lóópez-Ayala, M.E. Rincóón, Journal of Photochemistry and Photobiology A: Chemistry 222 (2011) 249–257.

[38] K.S.W. Sing, Journal of Porous Materials 2 (1995) 5–8.

[39] K. Lalitha, G. Sadanandam, V.D. Kumari, M. Subrahmanyam, B. Sreedhar, N.Y. Hebalkar, Journal of Physical Chemistry C 114 (2010) 22181–22189.

[40] C. Shifu, Z. Sujuan, L. Wei, Z. Wei, Journal of Nanoscience and Nanotechnology 9 (2009) 4397–4403.

[41] H. Bai, Z. Liu, D.D. Sun, International Journal of Hydrogen Energy 37 (2012) 13998–14008.

[42] M. Ashokkumar, International Journal of Hydrogen Energy 23 (1998) 427–438.

[43] K. Maeda, T. Ohno, K. Domen, Chemical Science 2 (2011) 1362–1368.

[44] H.J. Choi, M. Kang, International Journal of Hydrogen Energy 32 (2007) 3841–3848.

[45] J. Bandara, C.P.K. Udawatta, C.S.K. Rajapakse, Photochemical and Photobiological Sciences 4 (2005) 857–861.

[46] C. Wang, C. Shao, X. Zhang, Y. Liu, Inorganic Chemistry 48 (2009) 7261–7268.

[47] J.H. Pan, H. Dou, Z. Xiong, C. Xu, J. Ma, X.S. Zhao, Journal of Materials Chemistry 20 (2010) 4512–4528.

[48] J. Yu, Y. Hai, M. Jaroniec, Journal of Colloid and Interface Science 357 (2011) 223–228.

[49] N.L. Wu, M.S. Lee, International Journal of Hydrogen Energy 29 (2004) 1601–1605.

[50] J.M. Wu, Environmental Science and Technology 41 (2007) 1723–1728.

[51] G.K. Mor, O.K. Varghese, R.H.T. Wilke, S. Sharma, K. Shankar, T.J. Latempa, K.S. Choi, C.A. Grimes, Nano Letters 8 (2008) 1906–1911.

[52] H. Yu, J. Yu, S. Liu, S. Mann, Chemistry of Materials 19 (2007) 4327–4334.

[53] Y. Wu, G. Lu, S. Li, Catalysis Letters 133 (2009) 97–105.

[54] C. Bueno-Ferrer, S. Parres-Esclapez, D. Lozano-Castelló, A. Bueno-López, Journal of Rare Earths 28 (2010) 647–653.

[55] J.H. Pan, D.D. Sun, C. Lee, Y.J. Kim, W.I. Lee, Journal of Nanoscience and Nanotechnology 10 (2010) 4747–4751.

[56] G. Li, N.M. Dimitrijevic, L. Chen, T. Rajh, K.A. Gray, Journal of Physical Chemistry C 112 (2008) 19040–19044.

[57] Y.k. Su, C.m. Shen, H.t. Yang, H.l. Li, H.j. Gao, Transactions of Nonferrous Metals Society of China 17 (2007) 783–786(English Edition).